Scientia Iranica A (2015) 22(4), 1457–1469

Sharif University of Technology
Scientia Iranica
Transactions A: Civil Engineering
www.scientiairanica.com

A hybrid solid boundary treatment algorithm for smoothed particle hydrodynamics

A. Mahdavi* **and N. Talebbeydokhti**

Department of Civil and Environmental Engineering, Shiraz University, Shiraz, Iran.

Received 23 May 2014; received in revised form 6 October 2014; accepted 1 December 2014

KEYWORDS
SPH;
Solid boundary condition;
Free surface flow;
Dam break;
Sharp-crested weir.

Abstract. This study presents a new hybrid algorithm for treating solid walls in the context of a weakly-compressible SPH model. The basic concept is to fill an impervious region with some layers of dummy particles for improving the solution accuracy, and a single layer of repulsive particles to impose a no-penetration condition along the solid-fluid interface. The latter consists of a new repulsion mechanism that, unlike the well-known Lennard-Jones model, induces no pressure oscillation close to the wall. This hybrid boundary treatment technique is implemented in conjunction with a parameter-free SPH scheme to provide a Lagrangian solver for 2D Navier-Stokes equations. The accuracy of the model is verified by recourse to challenging numerical tests in free surface hydraulics, including a dam break surging over a dry bed, with and without obstacles, as well as a free falling water jet from a sharp-crested weir. Comparison with relevant numerical and/or experimental data from the literature shows fair agreement in each case.

1. Introduction

Smoothed Particle Hydrodynamics (SPH) is a mesh-free, Lagrangian scheme, invented for astrophysical simulations independently by Gingold and Monaghan [1], and Lucy [2]. In the course of development, the scheme has been successfully examined in a broad range of applications, including solid mechanics [3], complex free surface flows [4], and wave-structure interactions [5], among others. The interested reader is referred to the works of Liu and Liu [6], and Monaghan [7,8] for a comprehensive review of the relevant applications and theoretical background of the methodology.

Concerning free surface modeling, which is at the focus of this study, SPH has an elegant feature. It automatically delineates a free surface, no matter how complex it is in shape. The fluid continuum is decomposed into a finite set of particles that completely determine the state of the system at a discrete level. These particles are free to move, but only according to movement dictated by the governing equations of fluid motion. Wetting-drying fronts can, thus, be tracked straightforwardly, without extra effort, such as mapping [9] or remeshing techniques. These all highlight the Lagrangian nature of the method.

Although the SPH method has been proven efficient in capturing free surface boundaries, careful attention should be given to properly model solid walls that surround the flow region. Improper implementation of such solid interfaces may lead to serious contamination of the entire computational domain, and thus, to erroneous predictions. This may also cause numerical instability as time evolves. Besides, it is crucial to prevent unphysical penetration of fluid particles into the solid boundary.

Several methods have been proposed for dealing with solid boundaries in SPH. A number of well-known techniques are briefly revisited herein, from the

*. *Corresponding author. Mobile: +98 918 348 6596; Fax: +98 711 647 3161*
E-mail addresses: mahdavi@shirazu.ac.ir (A. Mahdavi); taleb@shirazu.ac.ir (N. Talebbeydokhti)

view point of their applicability, limitation, and merit. A very simple technique for treating solid walls can be constituted by considering the fact that a fluid particle approaching a solid wall experiences an elastic bounce, so that a fraction of its kinetic energy will be dissipated [10]. However, this technique reduces the solution accuracy, since it significantly distorts the flow field in the vicinity of solid boundaries [11].

Some authors have adopted the ghost particle technique to represent a solid wall [12,13]. To this end, additional particles are generated outside a solid boundary by instantaneously mirroring nearby fluid particles, with respect to that boundary line. These particles tend to mimic the solid boundary with density, pressure and velocity deduced from neighboring fluid particles. In this way, either free-slip or no-slip boundary condition can be implemented in the code. However, the position and the number of ghost particles may change every time step, leading to difficulties in computer implementation. Moreover, mirroring a particle, with respect to a boundary line, requires knowledge about local normal vectors to that boundary. This represents the main drawback of the approach, particularly in the presence of irregular boundaries or sharp edges.

In an alternative approach, dynamic particles are distributed in some two or more layers outside the solid boundary in a uniform or staggered pattern [5,14]. The position of dynamic particles remains fixed during the entire simulation time while their density and pressure are evolved similar to a real fluid particle, namely, by satisfying the mass conservation law and equation of state. Although this technique is very simple to implement, numerical experiments show the unphysical stick of fluid particles on the solid-fluid interface, as reported in [15].

According to the repulsive force method, a line of particles located along the solid-fluid interface exerts repulsion on the approaching fluid particles to prevent their penetration of the wall. Basically, these forces stem from inter-molecular potentials and act along the line connecting two particles. The Lennard-Jones force is an example [16]. Despite its ease of implementation, this technique produces high magnitude repulsion when inter-particle distance becomes very small. This, in turn, disturbs pressure distribution near the wall. Improved models to overcome this issue can be found in the works of Rogers and Dalrymple [17], and Shao et al. [18].

In the context of incompressible SPH, a number of techniques, such as mirror particles [19] and fixed wall particles [20], have been developed to implement the no-slip or free-slip, and Neumann boundary conditions for a solid boundary. More recently, Liu et al. [21] proposed an improved mirror particle that significantly enhances numerical accuracy and stability by reducing pressure oscillations in the vicinity of the solid wall.

When a fluid particle reaches a solid boundary, accuracy of the related SPH approximations decreases, since no particle exists outside the boundary to contribute in particle interaction. This is often referred to as the density deficiency problem in SPH literature [16]. In addition, some approaching fluid particles may penetrate a solid wall in an unphysical manner, leading to an artificial mass loss or even instability of computation.

This study aims to alleviate the above-mentioned issues by combining the dummy particles and a soft repulsive force model in favor of accurate flow predictions near the solid walls. This new hybrid boundary treatment is efficient and simple to implement. The organization of the paper is as follows: In section 2, the governing equations of fluid motion are provided. Section 3 briefly reviews the basics of SPH modeling, and subsequently proposes the hybrid boundary treatment in detail. Three numerical tests are considered in Section 4 to assess the validity of the method as adopted herein. These include simulation of a dam break surging over a dry bed, with and without obstacle, as well as a free falling water jet from a sharp-crested weir. The paper ends with concluding remarks and some ideas for further work in Section 5.

2. Governing equations

This study focuses on numerical solution of Navier-Stokes equations, employing a Lagrangian description of motion:

$$\frac{d\rho}{dt} = -\rho\vec{\nabla}.\vec{u}, \tag{1}$$

$$\frac{d\vec{u}}{dt} = -\frac{1}{\rho}\vec{\nabla}p + \vec{F}. \tag{2}$$

The above equations express the fundamental laws for conservation of mass and momentum, respectively in which, t is time, ρ is fluid density, $\vec{u}$ is flow velocity, p is pressure and $\vec{F}$ is the external force per unit mass, which typically includes contribution from gravity, $\vec{g}$, and repulsive boundary forces, as discussed later.

Owing to the Lagrangian nature of the SPH, it is possible to follow the trajectory of individual fluid parcels that advect with the flow. This feature may be considered the key advantage of the method, particularly in the presence of moving boundaries, such as a free surface. In other words, there is no need for a special free surface tracking scheme, such as volume of fluid. Moreover, the Lagrangian momentum equation contains no convection term and the position

of particles is simply updated as follows:

$$\frac{d\vec{x}}{dt} = \vec{u}, \tag{3}$$

where $\vec{x}$ denotes the time-dependent position of the fluid particle. The global flow motion is determined after integrating Eq. (3) in time for each fluid particle involved in the computation. It is common practice to take the SPH fluid as weakly-compressible. This assumption allows pressure to be uniquely determined from the density field by introducing an Equation Of State (EOS). It is worth mentioning that using an EOS considerably reduces the computational costs required to obtain the pressure field, since it eliminates the need for solving an extra Poisson equation, which constitutes an essential component of any incompressible SPH solver [22]. The Tait EOS is commonly chosen in dealing with free surface flows [4]. It is given by:

$$p = b_0 \left(\left(\frac{\rho}{\rho_0} \right)^{\gamma} - 1 \right), \tag{4}$$

where ρ_0 is the reference density of the fluid phase at atmospheric pressure ($\rho_0 = 1000$ kg/m^3 in what follows). The exponent, γ, is commonly taken as equal to 7 for free surface flows [13]. The coefficient, b_0, relates to the speed of sound, and it is selected such that allowable density variations stay to within 1% during the entire simulation time [23]. This requirement is consistent with the nature of assumed weakly-compressible fluid.

3. Numerical procedure

3.1. SPH discretization scheme

The basic idea behind the SPH technique is to decompose fluid continuum into a finite set of discrete Lagrangian particles, each carrying individual physical quantities and obeying the governing equations of fluid motion. These ever-changing particles are often initially distributed on a Cartesian lattice, forming an equally-spaced pattern. Detailed flow features can be described well by increasing the number of particles involved, but at the cost of increased computational time. Each particle is assigned a constant mass, m, though it occupies a time-dependent volume of space, $V = m/\rho$, due to density variations inherent in a weakly-compressible fluid.

The SPH particles essentially act as moving interpolation points. During flow evolution, the physical quantities associated with each particle are interpolated from the information at its neighbors, using smoothing kernel W as a weighting function. The neighboring particles for a generic particle, i, are those that locate within its support domain, which delineates a circle of radius, kh, centred at $\vec{x}_i$ for 2D problems. In other words, this defines a cutoff radius, kh, beyond which the kernel function vanishes.

Among several options proposed in the literature, a modified Gaussian kernel [13] is preferred here due to its improved stability aspects and enhanced code efficiency. This kernel function preserves the desired properties of the conventional Gaussian kernel, while possessing a certain compact support. It is given by:

$$W_{ij} = \begin{cases} \frac{\exp(-q_{ij}^2) - \exp(-k^2)}{2\pi h^2 \int_0^k \psi(\exp(-\psi^2) - \exp(-k^2))\, d\psi} & \text{for} \quad 0 \le q_{ij} \le k \\ 0 & \text{for} \quad q_{ij} > k \end{cases} \tag{5}$$

Here, $q_{ij} = |\vec{x}_{ij}|/h$, where $\vec{x}_{ij} = \vec{x}_i - \vec{x}_j$ is the vector connecting two interacting particles, i and j. In the present study, the characteristic smoothing length, h, is set equal to initial inter-particle spacing, denoted by Δ, also, $k = 3$ is adopted.

It is well known that the weakly-compressible SPH model suffers from unphysical fluctuations in the pressure and density fields. This may lead to tensile instability and even divergence in extreme cases. It is common practice to introduce an artificial viscosity term in order to prevent instabilities in a SPH simulation [4]. This term is supposed to embody the effect of real viscosity. Such effects tend to smooth out fluctuations in the fluid density, thereby, stabilizing the pressure field. The artificial viscosity term proposed by Monaghan [4] conserves both linear and angular momentum. However, it contains two adjustable parameters that need to be carefully calibrated before performing any simulation.

In this study, the density field is stabilized following the method proposed by Ferrari et al. [23], which is free from any calibration parameter and easy to implement. This technique employs the intrinsic numerical viscosity associated with the Rusanov flux [24] to remove spurious oscillations in the flow field. The continuity equation, therefore, reads:

$$\frac{d\rho_i}{dt} = \rho_i \sum_j V_j (\vec{u}_i - \vec{u}_j).\vec{\nabla}_i W_{ij} + \sum_j \left(c_{ij} V_j (\rho_j - \rho_i) \right) \vec{n}_{ij}.\vec{\nabla}_i W_{ij}, \tag{6}$$

where $\vec{n}_{ij} = \vec{x}_{ji}/|\vec{x}_{ji}|$. The SPH summation extends over the set of nearby particles (denoted by the subscript, j) whose locations fall within the support domain of particle, i. Therefore, all interacting pairs surrounded by a support domain have to be identified in each computational stage. This can be efficiently accomplished via the link list search algorithm [16]. The gradient of the smoothing kernel is computed with

respect to particle i and is denoted by $\vec{\nabla}_i W_{ij}$. It is easy to verify that $\vec{\nabla}_i W_{ij} = -\vec{\nabla}_j W_{ij}$.

Eq. (6) will set up sufficient penalization to remedy spurious density fluctuations, which is required to achieve a less noisy and more stable pressure field. Here, $c_{ij} = \max(c_i, c_j)$ determines the maximum wave celerity between each pair of interacting particles. With the assumption of weakly-compressible fluid, the wave celerity is explicitly linked to the pressure and density fields:

$$c_i = \left(\frac{b_0\gamma}{\rho_0}\right)^{\frac{1}{2}} \left(\frac{\rho_i}{\rho_0}\right)^{\frac{\gamma-1}{2}}, \tag{7}$$

which is actually $c_i = [(\partial p/\partial\rho)_i]^{1/2}$. Numerical experiment based on this approach confirmed that it avoids the highly disordered particles without requiring additional treatment to correct particle movement, such as XSPH [4].

Several SPH discretization schemes may be adopted for the pressure gradient term in the momentum equation. The scheme proposed by Hu and Adams [25] is utilized herein, where the momentum equation takes the following form:

$$\frac{d\vec{u}_i}{dt} = -\frac{1}{m_i}\sum_j \left(V_i^2 + V_j^2\right)\left(\frac{\rho_j p_i + \rho_i p_j}{\rho_i + \rho_j}\right)\vec{\nabla}_i W_{ij} + \vec{F}_i. \tag{8}$$

This approach introduces density-weighted inter-particle-averaged pressure in the velocity evolution equation. The antisymmetry property of the pressure gradient term in Eq. (8) guarantees that the pressure force between particles i and j is equal in magnitude, and opposite in sign to that between particles j and i, ensuring Newton's third law and the momentum conservation properties of the scheme.

3.2. A new hybrid solid boundary treatment

To accurately model a solid wall is a critical issue frequently investigated by the SPH community since the invention of the method. In fact, this represents a drawback of many particle methods compared to the conventional grid based techniques, which behave rather simply in the solid boundary treatment. A new hybrid solid boundary treatment algorithm is schematically depicted in Figure 1 and outlined in what follows.

To compensate for the density deficiency near a solid boundary, several layers of equally-spaced dummy particles are configured outside the boundary line. The number of layers depends on the radius of the support domain of an approaching fluid particle. For example, three layers of dummy particles are sufficient if $k = 3$. The dummy particles are assigned zero velocity to mimic a stationary solid wall. Other flow variables have to be properly assigned too. As shown by Adami et al. [26], the pressure of a stationary dummy particle, s, inspired by a single approaching fluid particle, a, is computed as:

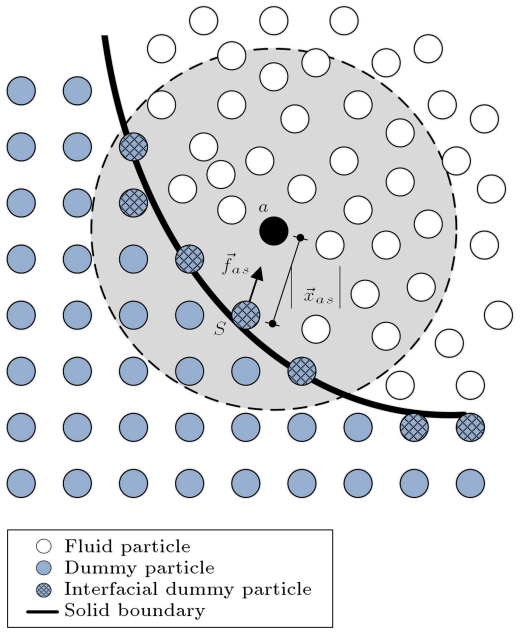

Figure 1. A sketch of the proposed algorithm for solid boundary treatment: The approaching fluid particle a (•) interacts with other fluid and dummy particles located within its support domain (the shaded area enclosed by dashed line) and experiences a repulsion, $\vec{f}_{as}$, from the interfacial dummy particle, s, if their inter-particle distance satisfies $|\vec{x}_{as}| \leq k_s h$.

$$p_s = p_a + \rho_a g(y_a - y_s). \tag{9}$$

The quantities corresponding to dummy and approaching fluid particles are denoted by respective subscripts, hereafter. The second term on the right hand side of Eq. (9) is the hydrostatic component caused by the elevation difference between the fluid and dummy particles, $y_a - y_s$. In the SPH convention, Eq. (9) is expressed as:

$$p_s = \frac{\sum_a \left(p_a + \rho_a g(y_a - y_s)\right) W_{sa} V_a}{\sum_a W_{sa} V_a}. \tag{10}$$

Eq. (10) constitutes a corrective kernel approximation for p_s in which the summations extend over the fluid particles that interact with particle s. The density of a dummy particle is computed from its pressure, according to EOS.

Although this method ensures a continuous flow field close to the boundary, under extreme circumstances, single approaching fluid particles could possibly penetrate through the solid walls and even escape the computational domain. To avoid this, the dummy particles located right on the solid-fluid interface are considered to exert repulsion on the approaching fluid

particles. These repulsive forces apply along the radial line connecting the two particles. Without loss of generality, both the fluid and repulsive particles are assigned an identical mass. As mentioned earlier, the commonly used model, i.e. the Lennard-Jones molecular force, is known to produce high-magnitude repulsions that cause pressure disturbances near the boundary region. This problem can be alleviated by applying a finite-magnitude repulsive force as proposed herein. Accordingly, the approaching fluid particle, a, experiences a force (per unit mass) due to the action of the single interfacial dummy particle, s, as given by:

$$\vec{f}_{as} = K\Psi(q_{as})\frac{\vec{x}_{as}}{|\vec{x}_{as}|^2}. \tag{11}$$

The factor, $K = 0.01b_0\gamma/\rho_0$, represents an estimate of the maximum force necessary to stop a fluid particle moving at the estimated maximum speed [7]. To avoid any wall penetration, function $\Psi(q_{as})$ is defined so that it monotonically increases as its argument, $q_{as} = |\vec{x}_{as}|/h$, decreases:

$$\Psi(q_{as}) = \begin{cases} \frac{\exp(-3q_{as}^2)-\exp(-3k_s^2)}{1-\exp(-3k_s^2)} & \text{for} \quad 0 \le q_{as} \le k_s \\ 0 & \text{for} \quad q_{as} > k_s \end{cases} \tag{12}$$

With this choice, the fluid particle experiences a finite-magnitude repulsion if its separation distance from a boundary particle is lower than the cutoff radius, $k_s h$, as referred to in Figure 1. The resultant force can be evaluated by summing the contributions from individual interfacial dummy particles whose set is denoted by IDPs. With this notation, the external force exerted on particle a, due to boundary effects, is evaluated as $\vec{F}_a = \sum_{s\in IDPs}\vec{f}_{as}$. Numerical experiments based on this formulation confirmed the formation of soft inter-particle repulsions without affecting near wall pressure distribution, provided that $k_s = 1 \sim 1.5$. The computational results were found to be globally insensitive to the value of k_s when it varies in the abovementioned range. The following computations are carried out with $k_s = 1.5$, unless otherwise stated.

It is worth mentioning that the repulsive particle technique can also be adopted for the case of rigid bodies interacting with an ambient fluid. This 2D movement is completely fluid-driven and characterized by translational-rotational degrees of freedom. The translational motion can be tracked by summing the forces exerted on the interfacial boundary particles for an entire body. This formalism enjoys the principle of equal and opposite action and reaction (i.e., $\vec{f}_{sa} = -\vec{f}_{as}$), due to the antisymmetry property of Eq. (11). The rotational motion is determined by the torque of the forces about the centre of mass of the rigid body. Following the work of Monaghan [7] and Khayyer et al. [27], it is straightforward to verify that both the linear and angular momentum of the system are preserved at the discrete level.

3.3. Time integration and stability consideration

The SPH flow equations form a system of Ordinary Differential Equations (ODEs) that can be explicitly marched in time to determine the dynamics of flow. Although any stable time integration scheme for ODEs may be implemented, in practice, those possessing a broader range of stability with a reduced memory requirement are usually preferred. Each flow equation can be cast in a generic form given by:

$$\frac{dU}{dt} = L(U). \tag{13}$$

In the present study, the conventional four stage Runge-Kutta method integrates resulting ODEs along the time axes. Although this scheme requires a higher numerical cost compared to the predictor-corrector scheme, it is more stable, and the computed time steps can be considerably longer than those allowed by the predictor-corrector scheme [28]. This time integrator is fully explicit and may be expressed in the compact form as:

$$\begin{aligned} U_i^{(k)} =& U_i^{(0)} + \alpha_k \Delta t\Big(L\left(U_i^{(k-1)}\right) + 2\beta_k L\left(U_i^{(k-2)}\right) \\ &+ 2\beta_k L\left(U_i^{(k-3)}\right) + \beta_k L\left(U_i^{(k-4)}\right)\Big) \\ &\text{for} \quad k = 1, ..., 4 \end{aligned} \tag{14}$$

with $U_i^{(0)} = U_i^n$ and $U_i^{n+1} = U_i^{(4)}$. Superscripts n and $n+1$ refer to the current and next time levels, respectively. The integration weighting coefficients satisfy $\alpha_3 = 2\alpha_1 = 2\alpha_2 = 6\alpha_4 = 1$, and the switching integers, β_k, are zero, except for $\beta_4 = 1$. For stability reasons, the magnitude of time step, Δt, should be constrained, according to the Courant-Friedrichs-Lewy (CFL) criterion, expressed as:

$$\Delta t = C_n \min_i\left(\frac{h}{c_i}, \frac{h}{|\vec{u}_i|}\right), \tag{15}$$

with C_n being the well-known CFL number.

4. Results and discussion

4.1. Dam break flooding over horizontal bed

In the first computational test, the present scheme is adopted to investigate the flow field generated by the collapse of a dam, and the subsequent impact of the propagating water front against a rigid vertical wall,

Table 1. A pseudo-code describing the steps involved in the computation of a dam break wave.

Step 1: Define problem geometry in terms of discrete particles for the fluid and surrounding solid boundaries. Particles are initially distributed in an evenly-spaced pattern.
Step 2: Initialize the system by assigning mass, density, velocity and pressure to each particle. Set $t = 0$.
Step 3: Perform link list search to identify all interacting pairs of particles, based on the current particle positions.
Step 4: Impose boundary conditions, Eqs. (10) and (11).
Step 5: Compute the rate of change of density for each fluid particle according to the mass conservation law, Eq. (6).
Step 6: Use EOS, Eq. (4), to evaluate pressure for each fluid particle.
Step 7: Compute the rate of change of velocity (acceleration) for each fluid particle according to the momentum conservation law, Eq. (8).
Step 8: Apply CFL criterion, Eq. (15), to dynamically adjust the time step, Δt.
Step 9: Based on the four stage Runge-Kutta method, Eq. (14), and the results already obtained in Steps 5 and 7, evolve density, velocity and position of fluid particles to the new time level, $t = t + \Delta t$. Note that Step 3 to Step 7 should be performed successively in each Runge-Kutta stage.
Step 10: Check whether the desired simulation time is achieved. If so, go to Step 11. Otherwise, jump to Step 3.
Step 11: Save the results for visualization or post-processing, End.

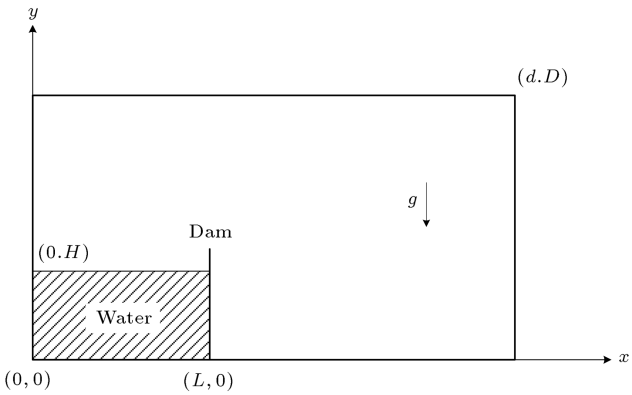

Figure 2. Schematic representation of dam break problem with $L = 2H$, $D = 3H$ and $d = 5.366H$ (after Zhou et al. [29]).

positioned downstream of the dam. This problem, despite its simple configuration, may offer useful insights into more complex hydrodynamic phenomena, such as wave-impact loading on coastal structures [5,14], or sloshing loads in fluid containers [18,28].

Figure 2 depicts a definition sketch of the problem, where a dam (wall) separates a column of water with height H and length $L = 2H$, from an initially dry tank in the downstream side. The Cartesian coordinate system (x, y) has its origin at the lower left corner of the tank, with the x-axis along the tank and the y-axis vertically upward. The same setup with $H = 0.6$ m has been investigated experimentally by Zhou et al. [29], and it is broadly accepted as a benchmark for verifying numerical schemes (e.g., [13,23,26,30]). Table 1 summarizes a pseudo-code describing the steps involved in this SPH simulation.

Initially, the water body behind the dam is under hydrostatic equilibrium with null velocity everywhere. The dam suddenly collapses at $t = 0$ and the water parcels have the opportunity to move in the tank under the action of gravity, producing in time a highly dynamical flow.

Figure 3 shows snapshots of the generated flow at different nondimensional times, $t(g/H)^{1/2}$ in which particles are colored according to their local nondimensional pressure, $p/(\rho_0 gH)$. This case involves a set of 96×192 fluid particles (corresponding to $H/\Delta = 96$). The released water impacts the right wall of the tank prior to $t(g/H)^{1/2} = 2.48$. The impact is accompanied by a narrow jet of water that runs up along the wall, overturns and falls back thereafter ($t(g/H)^{1/2} = 2.48$ to 5.47). The overturning tip then hits the underlying water ($t(g/H)^{1/2} = 6.18$), forming a big splash ($t(g/H)^{1/2} = 7.54$) that rebounds almost vertically in air. The splash curls and eventually plunges forward into the water body, giving rise to a highly distorted and broken free surface profile ($t(g/H)^{1/2} = 9.01$). The flow gradually becomes quiescent afterwards. The simulation was continued until $t(g/H)^{1/2} \approx 40$, which

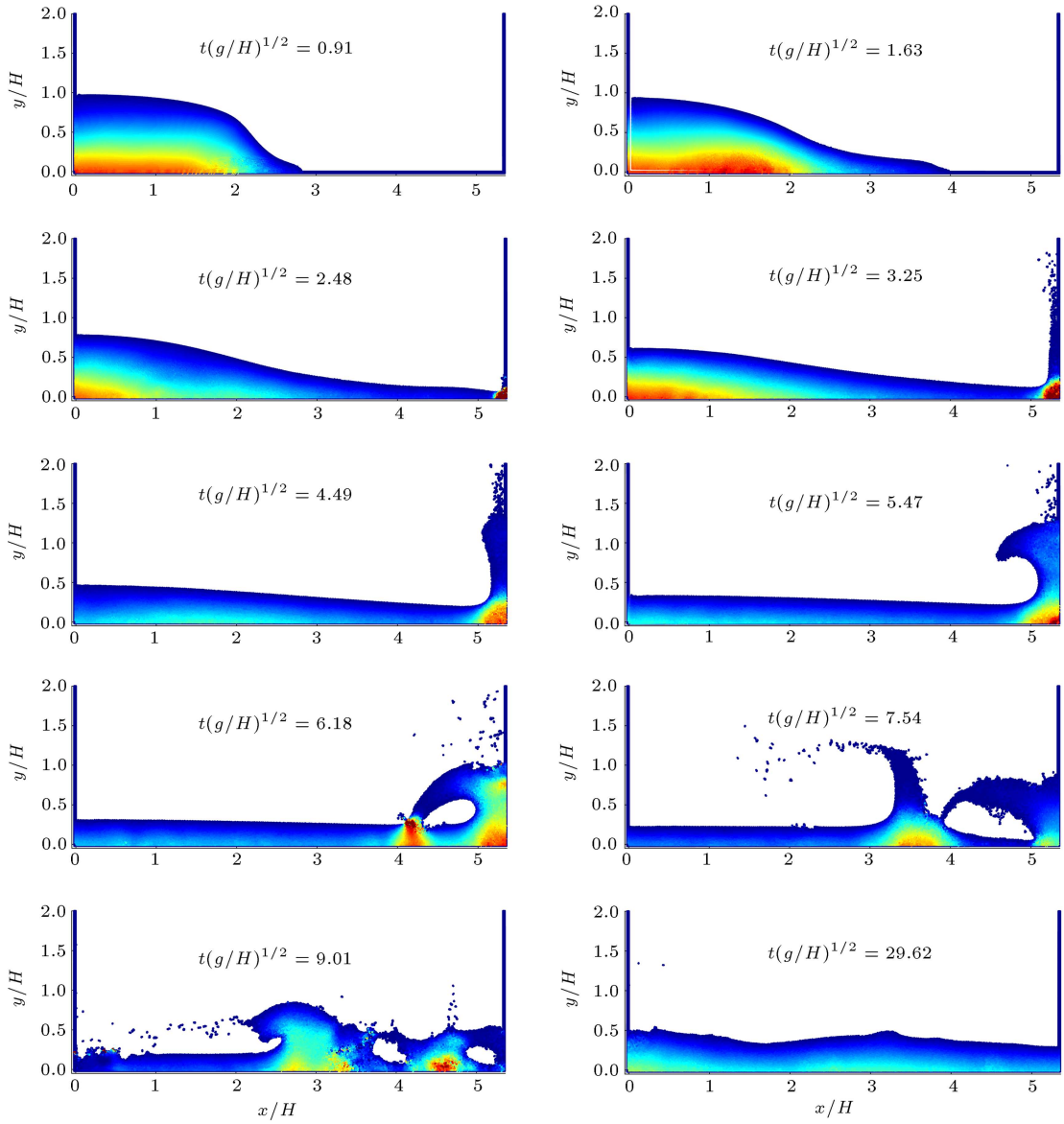

Figure 3. Evolution of free surface flow after break of a dam. The colormap varies from blue to red indicating the range of nondimensional pressure, $p/(\rho_0 g H)$, between zero and one.

covers several wave impacts on the tank walls. This ensures the long-term stability of the boundary treatment method proposed herein.

Figure 4 depicts a close-up view of the computed free surface profile for the instant at which the overturning jet hits the underlying water. Also shown in this figure is the numerical result obtained by the Boundary Element Method (BEM) at the same instant [13]. The BEM relies on the irrotational motion of inviscid fluid in the context of potential flow theory. From the qualitative aspects, both models agree fairly well in predicting the extent of entrapped cavity, as well as the location of the jet impact point.

A further verification has been provided by comparing water depth time series with experimental measurements and other numerical solutions in Figure 5.

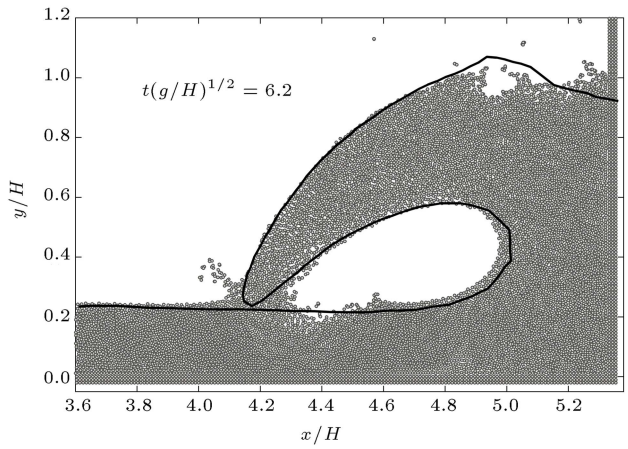

Figure 4. Present result (gray symbols) versus BEM computation [13] (solid line) for dam break problem.

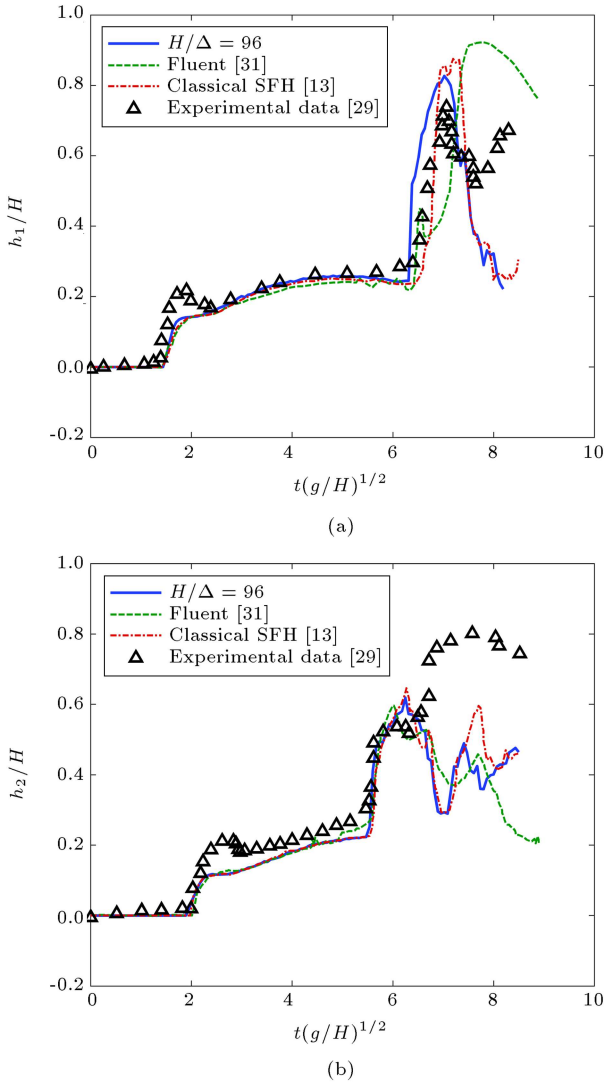

Figure 5. Time series of water depth at (a) $(x/H)_1 = 3.713$ and (b) $(x/H)_2 = 4.542$. Comparison between the present result ($H/\Delta = 96$) and other experimental and numerical approaches.

These include Fluent simulation results from [31] and classical SPH predictions from [13], which is computed based on periodic density renormalization. Two wave gauges were installed at $(x/H)_1 = 3.713$ and $(x/H)_2 = 4.542$ to record water depths, h_1 and h_2, during the whole experiment [29]. The evaluation of water depth has been carried out in the post-processing of SPH results by subtracting the height of the possibly present entrapped cavity from the total water level. This algorithm is motivated by the fact that the standard capacitive wave gauges installed in the experimental flume were sensitive to the wet part of the wire [13]. From Figure 5(a) and (b), it is evident that all numerical results satisfactorily agree with experimental measurements until the collapse of the entrapped air cavity. Afterwards, however, the experimental water depth reveals an increasing trend, but, the numerical

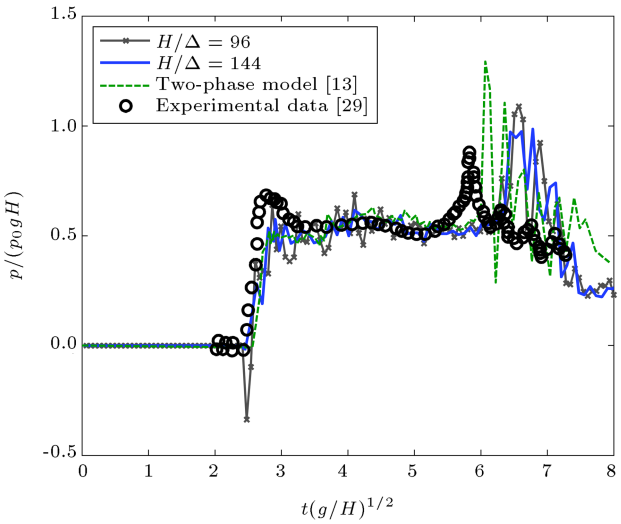

Figure 6. Time series of pressure at $y/H = 0.19$ on the right wall. The present results are computed for different particle resolutions ($H/\Delta = 96$, 144) and compared with other experimental and numerical approaches.

counterparts appear to decrease, except for Fluent predictions in case of h_1.

Figure 6 compares the computed pressure time series on the right wall with experimental data from [29] and two-phase SPH computation from [13]. The measuring point is positioned at $y/H = 0.19$ on the wall in accordance with the work of Adami et al. [26]. All fluid particles approaching this point contribute to computing the pressure through a corrective SPH interpolant, based on the aforementioned kernel function. The computed pressure profiles oscillate mostly around the experimental data, implying proper prediction of the main pressure plateau by the present model. As Figure 6 indicates, a finer particle resolution ($H/\Delta = 144$ corresponding to 144×288 fluid particles) noticeably reduces the magnitude of oscillations, which, in turn, produces a smoother pressure profile.

The experimental pressure profile is characterized by two peaks. The first pressure peak occurs when the advancing wave front hits the measuring point on the wall, while the second peak is due to the formation of the air cavity. The latter is slightly delayed because the air compressibility effect is not accounted for by the present single-fluid model. The delay is less pronounced in the case of the two-phase model, due to the inclusion of the air effect, though an overestimation of the second peak can be observed. On the other hand, the magnitude of this peak is fairly close to the experimental one for the present results, with $H/\Delta = 144$.

4.2. Dam break wave impinging on obstacle

This numerical test considers the problem of a dam break wave interacting with an obstacle block, as schematically depicted in Figure 7. One may regard

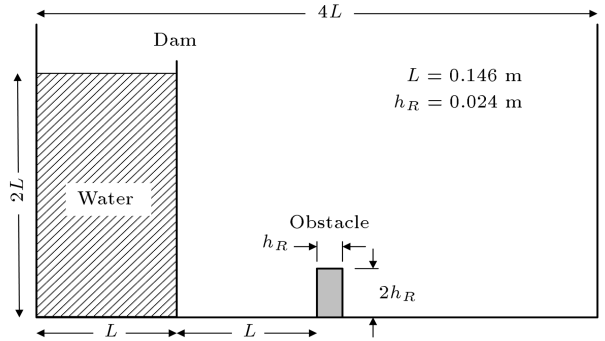

Figure 7. Schematic representation of dam break with obstacle (after Koshizuka et al. [32]).

the obstacle as a protecting dike that mitigates wave impact loads on the rigid structure that is resembled by the downstream wall of the tank. The same problem has been studied experimentally by Koshizuka et al. [32] and, later, numerically, by Larese et al. [33] via the Particle Finite Element Method (PFEM). The dam keeps a rectangular column of water with the width of L and height of $2L$ initially, at rest, and under hydrostatic pressure distribution. A bottom-mounted obstacle of dimension $h_R \times 2h_R$ is positioned downstream of the dam, at the middle of the tank. In the experimental setup, $L = 0.146$ m and $h_R = 0.024$ m were adopted. In the numerical setup, the fluid domain was discretized into 29×58 SPH particles.

Figure 8 depicts several snapshots of wave evolution after the sudden removal of the dam at $t = 0$. Also shown in this figure are photos from the physical experiment [32] and PFEM results [33] at the same time instants. The particle configuration at $t = 0.1$ s indicates an unphysical detachment of flow from the vertical wall on the left hand side. This spurious gap is efficiently removed by adopting a smaller cutoff radius, $k_s = 1$, as shown in Figure 8. Apart from this, however, the SPH predictions reveal an overall similar pattern for both $k_s = 1$ and 1.5 as flow evolves. The water front impinges on the obstacle after about $t = 0.1$ s and, subsequently, initiates a jet splash-up. Upon hitting the right wall of the tank, the bulk of the jet runs down and starts a reverse motion to completely inundate dry portions of the tank.

As expected, no particle penetration occurs during violent collisions between the fluid and solid phases. Also, individual fluid particles appear to instantaneously bounce back upon collision, without getting stuck to the solid faces. Such behavior again confirms, at least qualitatively, proper implementation of wall boundary conditions, as proposed in this study.

Referring to Figure 8, the wave profiles obtained from the present model match satisfactorily with both the experimental and PFEM results prior to $t = 0.4$ s. However, discrepancies arise between the numerical solutions and experimental data after this instant. Such differences can be mainly attributed to air entrapment effects (air cavity) in the experiment, which is not explicitly accounted for in either of these numerical schemes. On the other hand, the experimental results are reproduced well by the present model, whilst the fluid particles are being settled down in the tank. This is the case at $t = 1.0$ s, where the present model behaves rather better than PFEM in reproducing the experimental profile.

4.3. Flow over sharp-crested weir

The overflow water jets are highly complex to be numerically treated, due to the large deformation of the generated flow field and the presence of two simultaneous free surfaces (upper and lower nappe) in the air. From a numerical point of view, simulation of such overtopping jets requires the proper treatment of non-hydrostatic pressure fields triggered by rapidly varying flows. Moreover, the numerical model should be capable of efficiently capturing moving and arbitrary shaped boundaries along the water-air interface. From a practical point of view, the standard spillways are often shaped in accordance with the profile of a free jet falling from a sharp-crested weir.

This test is, therefore, aimed at comparing the results of the present SPH model with an empirically derived nappe profile for sharp-crested weirs, as reported in [34]. Accordingly, the geometry of the lower nappe may be delineated as:

$$\overline{Y} = -\overline{X} \ln \overline{X} \left(1 + \frac{1}{6}\overline{X}\right), \tag{16}$$

where $\overline{X} = 1.5(\overline{x}/\overline{h_0})$ and $\overline{Y} = 3.5(\overline{y}/\overline{h_0})$ refer to nondimensional coordinates characterizing the lower nappe trajectory; $\overline{h_0}$ is the head on the weir; and $\overline{x}, \overline{y}$ is the Cartesian coordinate system with the origin at the weir crest, being related to the previously defined coordinate system, as $\overline{x} = x - L$ and $\overline{y} = y - \overline{w}$, where $\overline{w}$ is the weir height. The head, $\overline{h_0}$, should be measured far enough upstream from the weir to suppress the streamline curvature effects near the weir crest.

To set up this SPH simulation, a reservoir, $L = 2.4$ m in length, is filled with water up to a height of $H = 0.6$ m. The water body is initially at rest and separated from a dry downstream channel via a vertical thin plate, whose upper half is suddenly removed at $t = 0$. The lower half of the plate remains fixed to the tank bottom because it is intended to serve as a sharp-crested weir; $\overline{w} = 0.3$ m in height. The procedure adopted herein was originally proposed by Ferrari [35]. This simulation involves a set of 96×384 fluid particles corresponding to $H/\Delta = 96$.

The flow field is entirely dominated by the mutual interaction of gravitational and inertial forces. Close examination of Figure 9 reveals that the lower nappe detaches from the weir plate at the upstream crest

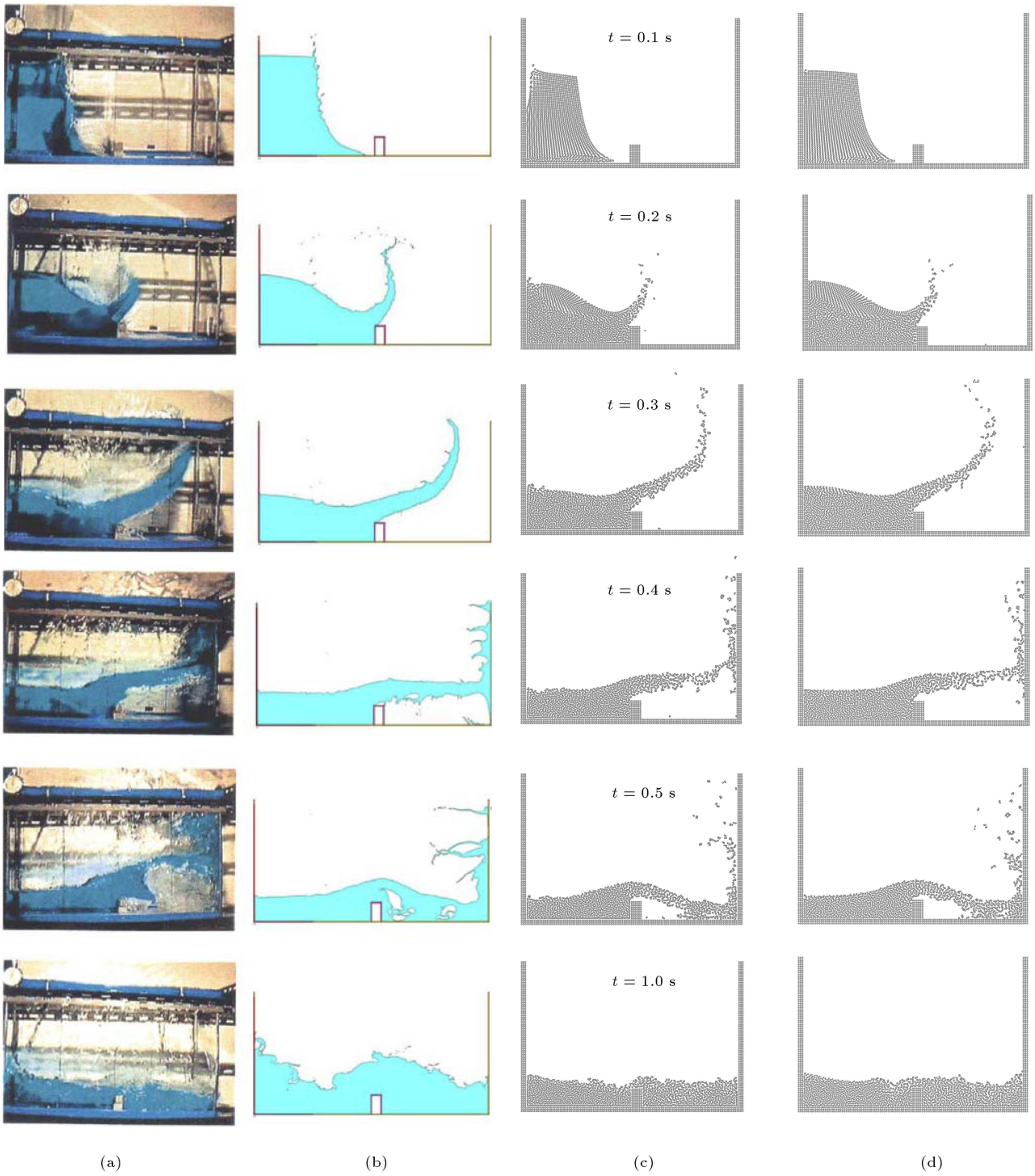

Figure 8. Experimental water profiles [32] (column a) versus PFEM [33] (column b), and present results for $k_s = 1.5$ (column c) and $k_s = 1$ (column d) at the same times.

edge, reaches its maximum altitude and then falls downwards. Concurrently, the overtopping jet develops freely in air before hitting the downstream bed at around $t = 0.28$ s. The impact is characterized by an increase in the local pressure field. After that, a portion of overtopped fluid initiates a reverse flow towards the weir, forming a vortical flow beneath the nappe ($t = 0.64$ to 2.5 s). The drawdown of the water surface at the weir site also produces a negative wave that gradually declines the reservoir level, while propagating upstream into the fluid at rest. Mathematically speaking, this flow field never reaches a purely steady state condition. Nevertheless, a quasi-steady behavior prevails at around $t = 1.0$ s, with a

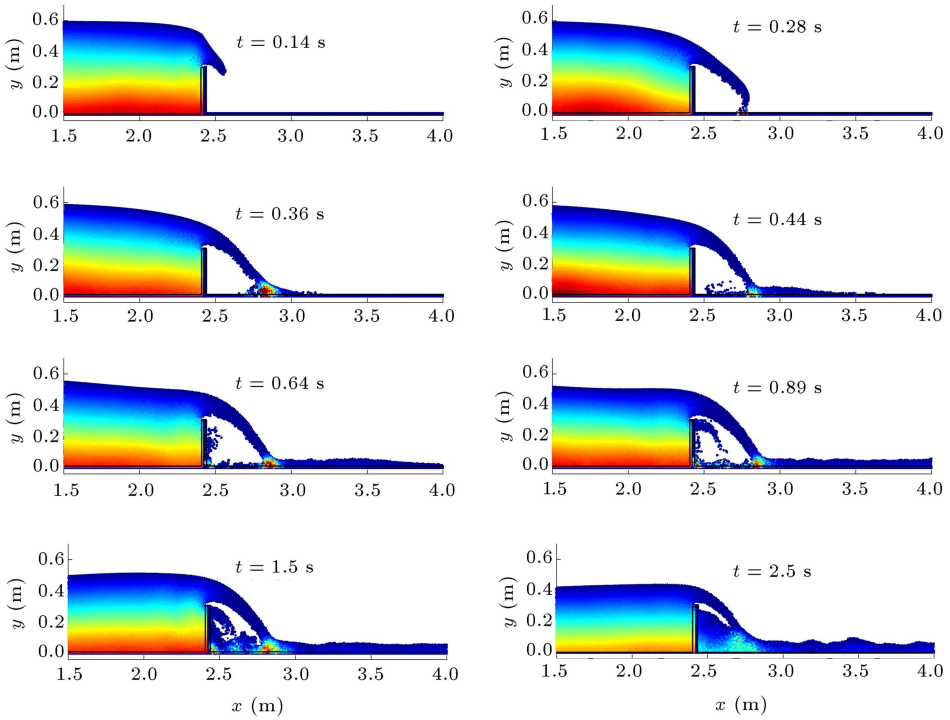

Figure 9. Evolution of nappe flow over a sharp-crested weir as predicted by the present model. The colormap varies from blue to red indicating the range of nondimensional pressure, $p/(\rho_0 g H)$, between zero and one.

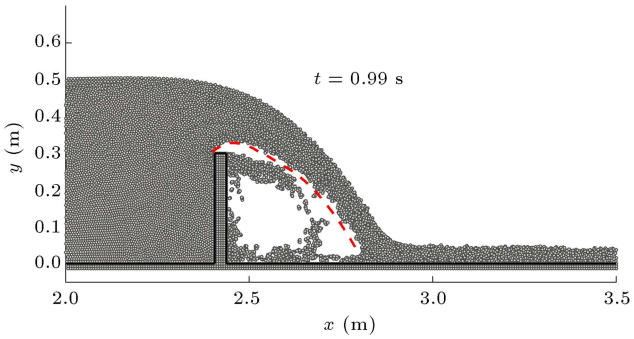

Figure 10. Comparison between the SPH solution (gray symbols) and the empirical lower nappe profile [34] (red dashed line).

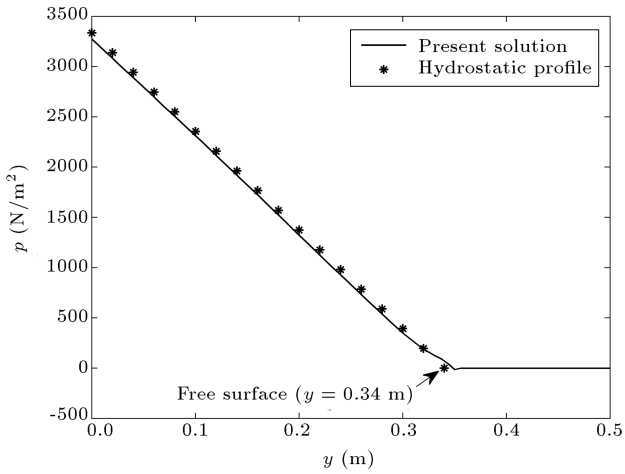

Figure 11. Pressure profile computed along $x = 0$ for $t = 10$ s versus exact linear hydrostatic profile.

corresponding head of $\overline{h_0} = 0.22$ m in the reservoir. This condition forms a basis for the comparison carried out in Figure 10 where a reasonably good agreement is achieved. Clearly, the aforementioned features associated with the lower nappe trajectory (detachment point, rising and falling limbs) are correctly captured by this weakly-compressible SPH model. The instantaneous discharge per unit length of the crest is found to be $q_{\text{weir}} = 0.198$ m^2/s, which agrees fairly well with the semi-empirical prediction, $q_{\text{weir}} = 0.203$ m^2/s, by the well known head-discharge formula, $q_{\text{weir}} = \frac{2}{3}\left(0.611 + 0.075\overline{h_0}/\overline{w}\right)\sqrt{2g}\,\overline{h_0}^{3/2}$.

It is to be noted that the numerical models relying on the hydrostatic pressure assumption fail to resolve such flow features, due to large streamline curvatures occurring in the nappe profile. Also, free falling jets tend to violate the underlying assumptions of depth-integrated flow solvers, such as the one developed in [36].

On the other hand, the flow in the reservoir eventually recovers hydrostatic equilibrium far away from the weir where the pressure field counterbalances the gravitational effect. Figure 11 compares the computed pressure distribution on the upstream wall of the reservoir with the linear hydrostatic profile. The SPH results, which refer to pressure at interfacial dummy particles along $x = 0$ for $t = 10$ s, are

in very close agreement with the theoretical pressure over flow depth. As expected, the computed pressures remain strictly zero for the interfacial particles located above the free surface level. These, again, confirm the accuracy of the solid boundary treatment algorithm proposed in this study.

5. Conclusion

A new hybrid algorithm was proposed for dealing with solid, impervious walls in SPH. For this purpose, solid regions were discretized with some layers of dummy particles to compensate for the density deficiency near the wall and to improve solution accuracy therein. The first layer of dummy particles, located right on the solid-fluid interface, was considered to produce the desired repulsion mechanism. Such a combination of boundary particles ensures not only a continuous flow field near the walls, but also no particle penetration through the solid faces. This hybrid method was incorporated into a parameter-free SPH scheme to achieve a more accurate pressure field. Motivated by its enhanced stability, an explicit multi-stage Runge-Kutta method was implemented for time-marching.

The efficiency of the present formulation was demonstrated through three numerical tests, each characterized by strongly deforming free surface and/or violent collisions between the fluid and solid wall. The cases studied include simulation of a dam break surging over a dry bed, with and without obstacles, in the downstream channel, as well as a free falling water jet from a sharp-crested weir.

This new boundary treatment is stable, easy to implement and introduces relatively small computational effort. Moreover, it offers flexibility in treating complex solid boundaries because no information about the boundary unit normal vectors is required. The proposed scheme can be extended to account for: (i) moving walls with prescribed motion, which may serve as wave makers in a numerical wave flume, and (ii) fluid-solid interactions, wherein the moving solid obeys rigid body motion with translational-rotational degrees of freedom. These are left as topics for future research work.

References

1. Gingold, R.A. and Monaghan, J.J. "Smoothed particle hydrodynamics-theory and application to non-spherical stars", *Monthly Notices of the Royal Astronomical Society*, **181**, pp. 375-389 (1977).
2. Lucy, L.B. "A numerical approach to the testing of the fission hypothesis", *The Astronomical Journal*, **82**, pp. 1013-1024 (1977).
3. Libersky, L.D., Petschek, A.G., Carney, T.C., Hipp, J.R. and Allahadi, F.A. "High strain Lagrangian hydrodynamics: A three-dimensional SPH code for dynamic material response", *Journal of Computational Physics*, **109**(1), pp. 67-75 (1993).
4. Monaghan, J.J. "Simulating free surface flows with SPH", *Journal of Computational Physics*, **110**(2), pp. 399-406 (1994).
5. Gómez-Gesteira, M. and Dalrymple, R.A. "Using a three-dimensional smoothed particle hydrodynamics method for wave impact on a tall structure", *Journal of Waterway, Port, Coastal, and Ocean Engineering*, **130**(2), pp. 63-69 (2004).
6. Liu, M.B. and Liu, G.R. "Smoothed particle hydrodynamics (SPH): An overview and recent developments", *Archives of Computational Methods in Engineering*, **17**(1), pp. 25-76 (2010).
7. Monaghan, J.J. "Smoothed particle hydrodynamics", *Reports on Progress in Physics*, **68**(8), pp. 1703-1759 (2005).
8. Monaghan, J.J. "Smoothed particle hydrodynamics and its diverse applications", *Annual Review of Fluid Mechanics*, **44**, pp. 323-346 (2012).
9. Mahdavi, A., Hashemi, M.R. and Talebbeydokhti, N. "A localized differential quadrature model for moving boundary shallow water flows", *Journal of Hydraulic Research*, **50**(6), pp. 612-622 (2012).
10. Souto-Iglesias, A., Pérez-Rojas, L. and Zamora Rodríguez, R. "Simulation of anti-roll tanks and sloshing type problems with smoothed particle hydrodynamics", *Ocean Engineering*, **31**(8-9), pp. 1169-1192 (2004).
11. Souto-Iglesias, A., Delorme, L., Pérez-Rojas, L. and Abril-Pérez, S. "Liquid moment amplitude assessment in sloshing type problems with smooth particle hydrodynamics", *Ocean Engineering*, **33**(11), pp. 1462-1484 (2006).
12. Randles, P.W. and Libersky, L.D. "Smoothed particle hydrodynamics: Some recent improvements and applications", *Computer Methods in Applied Mechanics and Engineering*, **139**(1), pp. 375-408 (1996).
13. Colagrossi, A. and Landrini, M. "Numerical simulation of interfacial flows by smoothed particle hydrodynamics", *Journal of Computational Physics*, **191**(2), pp. 448-475 (2003).
14. Crespo, A.J.C., Gómez-Gesteira, M. and Dalrymple, R.A. "3D SPH simulation of large waves mitigation with a dike", *Journal of Hydraulic Research*, **45**(5), pp. 631-642 (2007).
15. Gómez-Gesteira, M., Rogers, B.D., Dalrymple, R.A. and Crespo, A.J. "State-of-the-art of classical SPH for free-surface flows", *Journal of Hydraulic Research*, **48**(S1), pp. 6-27 (2010).
16. Liu, G.R. and Liu, M.B., *Smoothed Particle Hydrodynamics: A Meshfree Particle Method*, World Scientific, Singapore (2003).
17. Rogers, B.D. and Dalrymple, R.A. "SPH Modeling of tsunami waves", *In Advanced Numerical Models*

for Tsunami Waves and Runup, World Scientific, Singapore (2008).

18. Shao, J.R., Li, H.Q., Liu, G.R. and Liu, M.B. "An improved SPH method for modeling liquid sloshing dynamics", *Computers and Structures*, **100**, pp. 18-26 (2012).
19. Lo, E.Y.M. and Shao, S.D. "Simulation of near-shore solitary wave mechanics by an incompressible SPH method", *Applied Ocean Research*, **24**, pp. 275-286 (2002).
20. Shao, S.D. and Lo, E.Y.M. "Incompressible SPH method for simulating Newtonian and non-Newtonian flows with a free surface", *Advances in Water Resources*, **26**, pp. 787-800 (2003).
21. Liu, X., Xu, H., Shao, S.D. and Lin, P. "An improved incompressible SPH model for simulation of wave-structure interaction", *Computers and Fluids*, **71**, pp. 113-123 (2013).
22. Ghadampour, Z., Talebbeydokhti, N., Hashemi, M.R., Nikseresht, A.H. and Neill, S.P. "Numerical simulation of free surface mudflow using incompressible SPH", *Iranian Journal of Science and Technology, Transactions of Civil Engineering*, **37**(C1), pp. 77-95 (2013).
23. Ferrari, A., Dumbser, M., Toro, E.F. and Armanini, A. "A new 3D parallel SPH scheme for free surface flows", *Computers and Fluids*, **38**, pp. 1203-1217 (2009).
24. Toro, E.F. *Riemann Solvers and Numerical Methods for Fluid Dynamics*, 3th Edn., Springer, Germany (2009).
25. Hu, X.Y. and Adams, N.A. "A multi-phase SPH method for macroscopic and mesoscopic flows", *Journal of Computational Physics*, **213**(2), pp. 844-861 (2006).
26. Adami, S., Hu, X.Y. and Adams, N.A. "A generalized wall boundary condition for smoothed particle hydrodynamics", *Journal of Computational Physics*, **231**(21), pp. 7057-7075 (2012).
27. Khayyer, A., Gotoh, H. and Shao, S.D. "Corrected incompressible SPH method for accurate water-surface tracking in breaking waves", *Coastal Engineering*, **55**, pp. 236-250 (2008).
28. Delorme, L., Colagrossi, A., Souto-Iglesias, A., Zamora-Rodriguez, R. and Botia-Vera, E. "A set of canonical problems in sloshing, Part I: Pressure field in forced roll-comparison between experimental results and SPH", *Ocean Engineering*, **36**(2), pp. 168-178 (2009).
29. Zhou, Z.Q., Kat, J.O.D. and Buchner, B. "A nonlinear 3D approach to simulate green water dynamics on deck", In *7th International Conference on Numerical Ship Hydrodynamics*, Nantes (1999).
30. Khayyer, A., Gotoh, H. and Shao, S.D. "Enhanced predictions of wave impact pressure by improved incompressible SPH methods", *Applied Ocean Research*, **31**(2), pp. 111-131 (2009).
31. Abdolmaleki, K., Thiagarajan, K.P. and Morris-Thomas, M.T. "Simulation of the dam break problem and impact flows using a Navier-Stokes solver", In *15th Australasian Fluid Mechanics Conference*, Sydney (2004).
32. Koshizuka, S., Tamako, H. and Oka, Y. "A particle method for incompressible viscous flow with fluid fragmentation", *Computational Fluid Dynamic Journal*, **4**, pp. 29-46 (1995).
33. Larese, A., Rossi, R., Oñate, E. and Idelsohn, S.R. "Validation of the particle finite element method (PFEM) for simulation of free surface flows", *Engineering Computations*, **25**(4), pp. 385-425 (2008).
34. Vischer, D.L. and Hager, W.H., *Dam Hydraulics*, Wiley, UK (1998).
35. Ferrari, A. "SPH simulation of free surface flow over a sharp-crested weir", *Advances in Water Resources*, **33**, pp. 270-276 (2010).
36. Mahdavi, A. and Talebbeydokhti, N. "Modeling of non-breaking and breaking solitary wave run-up using shock-capturing TVD-WAF scheme", *KSCE Journal of Civil Engineering*, **15**(6), pp. 945-955 (2011).

Biographies

Ali Mahdavi received a BS degree in Civil Engineering from Shahid Chamran University, Ahvaz, Iran, in 2004, and an MS degree in Hydraulic Structures, in 2008, from Shiraz University, Iran, where he is currently a PhD degree student in the Department of Civil and Environmental Engineering. His research interests include mathematical modeling in groundwater and free surface hydraulics.

Nasser Talebbeydokhti is Professor of Hydraulic and Environmental Engineering in the Department of Civil and Environmental Engineering at Shiraz University, Iran, where he is currently head of the Environmental Research and Sustainable Development Center. He has published more than 80 journal papers and 150 conference papers. His main areas of interest include: hydraulic engineering, sediment transport, environmental engineering and hydraulic structures. Professor Talebbeydokhti is Editor-in-Chief of the Iranian Journal of Science and Technology, as well as Associate Editor for many other Iranian journals.